Highly efficient CO_2 electroreduction to formate using Bismuth nanodots within ZIF-8 scaffold

Usman, Muhammad; Suliman, Munzir H.; Abdinejad, Maryam; Kok, Jesse; Naji, Hussain Al; Helal, Aasif; Yamani, Zain H.; Centi, Gabriele

DOI
10.1016/j.ccst.2025.100450

Publication date
2025

Document Version
Final published version

Published in
Carbon Capture Science and Technology

Citation (APA)
Usman, M., Suliman, M. H., Abdinejad, M., Kok, J., Naji, H. A., Helal, A., Yamani, Z. H., & Centi, G. (2025). Highly efficient CO_2 electroreduction to formate using Bismuth nanodots within ZIF-8 scaffold. *Carbon Capture Science and Technology*, *16*, Article 100450. https://doi.org/10.1016/j.ccst.2025.100450

Carbon Capture Science & Technology 16 (2025) 100450

Contents lists available at ScienceDirect

Carbon Capture Science & Technology

journal homepage: www.elsevier.com/locate/ccst

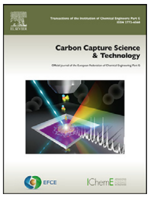

Full Length Article

Highly efficient CO_2 electroreduction to formate using Bismuth nanodots within ZIF-8 scaffold

Muhammad Usman[a,*], Munzir H. Suliman[a], Maryam Abdinejad[b,c], Jesse Kok[b], Hussain Al Naji[d], Aasif Helal[a], Zain H. Yamani[a], Gabriele Centi[e]

[a] Interdisciplinary Research Center for Hydrogen Technologies and Carbon Management (IRC-HTCM), King Fahd University of Petroleum & Minerals (KFUPM), Dhahran 31261, Saudi Arabia
[b] Department of Chemical Engineering, Delft University of Technology, 9 van der Maasweg, Delft, 2629HZ, the Netherlands
[c] Department of Energy Conversion and Storage, Technical University of Denmark, 2800 Kgs. Lyngby, Denmark
[d] Research and Development Center, Saudi Aramco, Dhahran 31311 Saudi Arabia
[e] Department of ChiBioFarAm, University of Messina, v.le F. Stagno D'Alcontres 31, Messina 98166, Italy

ARTICLE INFO

Keywords:
CO_2 conversion
eCO_2RR
Formic acid
Formate
Bi-Zn catalysts
Flow cell
MEA cell
Affordable and clean energy
Climate action

ABSTRACT

Zeolitic imidazolate frameworks (ZIFs) based electrocatalysts for CO_2 reduction offer unique possibilities for developing advanced materials for this reaction due to their ordered nanoporosity and pore environments, tunable characteristics and high affinity for CO_2. Still, they were not investigated sufficiently. In this study, we developed a Bismuth nanodots embedded Zeolitic Imidazolate Framework-8 (BND-ZIF-8) electrocatalyst via a one-pot synthesis method for the electrochemical CO_2 reduction reaction (eCO_2RR). Comprehensive spectroscopic and electrochemical characterization confirmed the successful integration of Bismuth into the ZIF-8 matrix. The electrocatalytic performance of the BND-ZIF-8 was assessed in multiple reactor typologies such as H-cell, flow cell, and membrane electrode assembly (MEA) setups. Remarkable differences in the performances in the three cell configurations are evidenced. Notably, the MEA configuration exhibited a marked enhancement in formate selectivity, achieving a Faradic efficiency (FE) of up to 91 % at a current density of -150 mA cm^{-2}. This work underscores the potential of Bi-ZIF-8 in advancing eCO_2RR while remarking on the crucial importance of the appropriate type of electrocatalytic experiments in assessing the material performance.

Introduction

The development of novel advanced functional materials to reuse CO_2 industrial emissions is still an open research question (Xu et al., 2015; Zhao et al. 2020; Garba et al. 2021; Centi and Perathoner 2023; Usman et al. 2023). The electrochemical reduction of carbon dioxide (eCO_2RR) stands out for its potential to transform chemical and fuel production while significantly contributing to climate change mitigation (Morales-Guio et al. 2018; Wu et al. 2019; Li et al. 2020; Wang et al. 2020). Liquid products like formate ($HCOO^-$)/formic acid (HCOOH) are particularly attractive outcomes of eCO_2RR, offering higher energy densities and easier storage and distribution compared to gaseous products (Costentin, Robert and Savéant 2013; Francke, Schille and Roemelt 2018; Abdinejad, Subramanian, Motlagh, Noroozifar, Duangdangchote, Neporozhnii, Ripepi, Pinto, Li, Tang, et al. 2023). With an annual global production of approximately one Mtons, formic acid supports a wide range of applications, including chemical manufacturing, sanitation, textile processing, and antiseptics (Lee et al. 2015; Schiffer and Manthiram 2017). However, the perspective in the use of formic acid is of a fast increase in the market, being a promising hydrogen carrier due to its ability to remain in liquid form at ambient conditions, its high hydrogen density (53 g H_2 per litre of HCOOH), and its low toxicity (Boddien et al. 2010). In addition, formic acid is a valuable feed for advanced fuel cells .(Shen et al. 2022; Suliman, Yamani and Usman 2023)

Metal-organic frameworks (MOFs), (Yaghi, Kalmutzki and Diercks 2019; Sathiyan et al. 2023; Usman and Suliman 2023; Suliman, Al Naji and Usman 2024) covalent organic frameworks (COFs), (Alenazi et al. 2025) and bimetallic compounds (Suliman et al. 2025; Usman et al. 2025) have been extensively studied for their potential in eCO_2RR. MOFs, in particular, feature tunable porous structures and coordination networks that make them promising CO_2 adsorbents and enhance mass transfer, which is advantageous for catalysis (Furukawa et al. 2013; Sun et al. 2021). Among them, Zeolitic Imidazolate Framework-8 (ZIF-8) is formed through the coordination of zinc ions (Zn^{2+}) with 2-methylimidazole (2mIm), creating a porous scaffold

---

* Corresponding author.
E-mail address: muhammadu@kfupm.edu.sa (M. Usman).

https://doi.org/10.1016/j.ccst.2025.100450
Received 4 April 2025; Received in revised form 26 May 2025; Accepted 29 May 2025

that has attracted attention for energy conversion applications due to its unique structure, stability, conductivity, and large surface area (Troyano et al. 2019; Bergaoui et al. 2021; Askarisarvestani et al. 2022; Song et al. 2024).

The incorporation of imidazole-containing ligand-metal coordination has been shown to enhance charge density, thereby improving the ability to bind and activate CO_2 for reduction (Zulkifli, Lim and Teh 2022). The synergistic effects of ZIF-8, and metal-based nanoparticles can further enhance catalytic efficiency in CO_2 reduction (Cho et al. 2023; Israr et al. 2024). Bismuth, in particular, is well-known for its selectivity towards formate production (Deng et al. 2019; Gao et al. 2019; Fan et al. 2020; Yao et al. 2021; Abdinejad, Subramanian, Motlagh, Noroozifar, Duangdangchote, Neporozhnii, Ripepi, Pinto, Li and Tang 2023; Yang et al. 2023; Li et al. 2024; Mahbub et al. 2024). Although Bismuth and ZIF-based systems, along with organic ligand functionalization, have demonstrated significant potential in electrocatalysis, there remains a need for further exploration into incorporating high-density active metals onto ZIFs scaffold for eCO_2RR. This could lead to the development of pre-catalysts with improved catalytic activity and selectivity, an area that remains underexplored. Furthermore, the performance of these catalysts in different electrolyzer configurations for eCO_2RR has yet to be comprehensively investigated.

In this work, we designed a high-dispersion, high density Bismuth nanodots incorporated into ZIF-8 for CO_2 electroreduction to formate, demonstrating promising activity and selectivity (Jiang et al. 2023). Unlike previous studies, which primarily focus on multi-step reactions to fabricate Bismuth nanodots MOFs for eCO_2RR, our work introduces a streamlined, one-step method for synthesizing Bismuth nanodots, enabling selective conversion of CO_2 to formate. This approach eliminates the need for complex post-treatment processes and enhances formate selectivity at low eCO_2RR overpotentials. The catalytic performance of Bi-ZIF-8 was systematically compared with ZIF-8 across various electrolyzer configurations, including H-cells, flow cells, and membrane-electrode assemblies (MEA). The results evidence the paramount role of using the appropriate cell configurations in evaluating the electrocatalytic performances and, thus, how assessing the performances of the electrocatalytic materials cannot leave aside the role of the reactor/electrode configuration and the associated change in mass transfer limitations. On the other hand, these evaluations also underscore the economic viability and practical potential of Bi-ZIF-8 for the electrocatalytic conversion of CO_2 to formate.

Results and discussion

Synthesis and structural characterizations of bismuth nanodots on ZIF-8 surfaces

ZIF-8 nanoparticles were functionalized with Bismuth nanodots through a reduction reaction to form Bi-ZIF-8. The process began by dispersing Bismuth ions in ZIF-8 aqueous solution, followed by the addition of sodium borohydride ($NaBH_4$) to the mixture. This step effectively reduced the Bismuth ions, leading to the formation of uniformly distributed Bismuth nanodots (BND) on ZIF-8. This method enabled the synthesis of large quantities of Bismuth nanodots incorporated in the ZIF-8 (BND/ZIF-8) under mild conditions, eliminating the need for complex equipment or high-temperature processes (Figure S1), where the prefix S indicates data reported in the Supplementary Info.

High-resolution transmission electron microscopy (HRTEM) revealed visible black dots corresponding to Bi, with a d-spacing of 0.33 nm (Fig. 1a). The particle size ranges from 2 to 8 nm is shown in Figure S2. Field emission scanning electron microscope (FESEM) in Fig. 1b further confirmed the formation of Bi-ZIF-8, showing the cubic crystal structure of ZIF-8 without the evident presence of Bi particles. Energy dispersive X-ray (EDX) analysis confirmed the presence of Zn, C, N, and Bi, while elemental mapping (Figure S3) demonstrated a uniform distribution of these elements throughout the Bi-ZIF-8 structure.

X-ray diffraction (XRD) results confirm the formation of Bi-ZIF-8. They showed crystalline reflections corresponding to ZIF-8, matching the standard Bi reference peaks (Fig. 1c). X-ray photoelectron spectroscopy (XPS) provided additional insights into the surface composition and chemical states of the Bi-ZIF-8 sample. The survey spectrum confirmed the presence of Zn, C, N, and O from ZIF-8, with an additional Bi peak observed (Fig. 1d and Figure S4). The C 1 s spectrum displayed two main peaks for C–C and ($C = O$, $C = N$) at binding energies of 283 eV and 286 eV, respectively. Moreover, the Zn spectrum (Figure S4b) showed peaks at binding energies of 1022 eV and 1045 eV, corresponding to Zn $2p_{3/2}$ and Zn $2p_{1/2}$, respectively. while the XPS of Bi 4f peaks for elemental bismuth are found around 157 eV (Bi 4f7/2) and 163 eV (Bi 4f5/2), corresponding to the 0 oxidation state (Bi(0)). In Bismuth oxide, the Bi 4f peaks shift to higher binding energies, with the Bi 4f7/2 peak around 158–160 eV and the Bi 4f5/2 peak around 164–166 eV, indicating that Bismuth is in the +3 oxidation state (Bi(III)) (Figure S4c). The main difference is that for Bismuth oxide, an O 1 s peak appears around 529–531 eV, representing the oxygen in the oxide, while there is no oxygen peak in the XPS of elemental Bismuth. In Fig. 1e, we can see the O 1 s peaks in the XPS results. Here, we observe a mixture of both Bismuth and Bismuth oxide (Figure S4d). These XPS results further confirm the successful dispersion of Bi within the ZIF-8 framework. This task was further validated using FTIR spectroscopy on ZIF-8 and Bi-ZIF-8 (Figure S5). The results are consistent with the literature, showing similar IR spectra (Chakraborty et al. 2024).

The surface areas of ZIF-8 and Bi-ZIF-8 were measured using a Brunauer-Emmett-Teller (BET) method (Fig. 1e). ZIF-8 exhibited a high surface area typical of MOFs, around 1750 m^2/g. After loading Bismuth nanodots, the surface area slightly decreased to ~1650 m^2/g for 5 % Bi-ZIF-8 and ~1580 m^2/g for 10 % Bi-ZIF-8, indicating successful Bi nanoparticle incorporation into the ZIF-8 framework. Further increases in Bi loading led to more significant reductions in surface area, reaching ~1100 m^2/g and ~950 m^2/g for 15 % and 20 % Bi-ZIF-8, respectively.

Electrochemical reduction of CO_2

The electrocatalytic activity of Bi-ZIF-8 for CO_2 reduction was evaluated using different reactor configurations for the crucial role they have in determining the performances and validating the effectiveness of the electrocatalysts (Ampelli et al. 2023). The first series of tests were realized using a gas-tight two-compartment H-cell with a 0.5 M $KHCO_3$ aqueous solution.

Electrocatalytic reduction of CO_2 using H–Cell

In the H–Cell, exposing the electrocatalysts to CO_2 compare to nitrogen increases current density with a remarkable shift to more positive potentials (Fig. 2a). The products of the reaction were periodically sampled from the cathodic chamber headspace and analyzed by gas chromatography (GC-BID). Additionally, the liquid sample was analyzed using proton nuclear magnetic resonance (^1H NMR). Using Bi-ZIF-8, only two gaseous products, H_2 and CO, were detected, along with formate as the liquid product.

Chronoamperometry tests at constant applied potentials ranging from −0.7 to −1.5 V vs reversible hydrogen electrode (RHE) were made to determine the optimal potential for eCO_2RR (Figure S6). The highest selectivity to CO was observed at −0.7 V vs RHE onset potential in with higher selectivity to CO (FE_{CO}) is about 50 % (Fig. 2b). At more negative potentials, the current density increased linearly, with formate emerging as the predominant product. At −1.3 V vs RHE, the formate selectivity is maximum, reaching a value of about 63 %, while the current density reached −50 mA cm^{-2}. ZIF-8 without Bi produces CO (Figure S7), while Bismuth with ZIF-8 produces formate, remarking on the role of Bismuth in promoting formate formation.

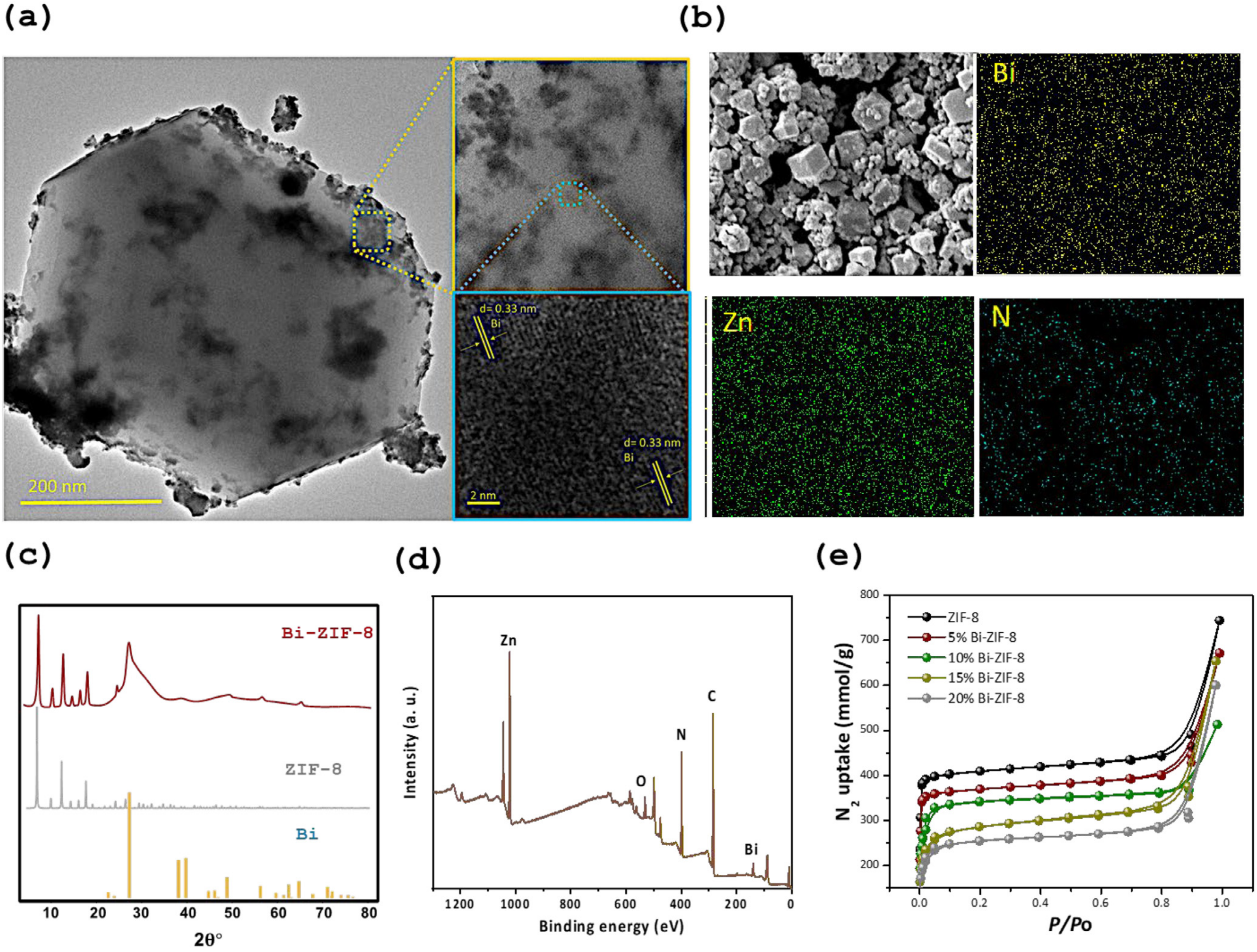

Fig. 1. (a) HRTEM of Bi-ZIF-8 (including d-spacing of Bi nanodots). (b) FESEM of Bi-ZIF-8 with elemental mapping. (c) XRD reference comparison of Bi, ZIF-8, and Bi-ZIF-8. (d) XPS survey spectrum of Bi-ZIF-8. (e) Brunauer-Emmett-Teller (BET) isotherm comparison of ZIF-8 and Bi-ZIF-8 with the concentration ratio of 5 % to 20 % of Bi.

The electrochemical surface area (ECSA) was determined by analyzing the rate of electron transfer between the solid support and catalysts using cyclic voltammograms (CVs) at various scan rates ranging from 50 to 250 mV/s for ZIF-8 and Bi-ZIF-8 are shown in Figure S8. The ECSA for various loadings of Bismuth in ZIF-8 are shown in Figure S9. The linear relationship between the reduction peak currents and the scan rate mV/s is shown in Fig. 2c indicates that Bi-ZIF-8 has a larger active surface area and higher electron transfer rate compared to ZIF-8 (10 mF cm^{-2} vs 0.9 mF cm^{-2}). This enhancement is attributed to the improved electron transfer and increased electrochemically active surface area of Bi-ZIF-8, which facilitates better adsorption of eCO_2RR intermediates on the catalyst surface, potentially leading to the better catalytic performance of Bi-ZIF-8.

The kinetics of the electrochemical processes were further analyzed using Electrochemical Impedance Spectroscopy (EIS) (Fig. 2d). The results demonstrate a charge transfer resistance (R_{ct}) of 160 Ω cm^2 for the ZIF-8 electrode and 10 Ω cm^2 for the Bi-ZIF-8 electrode, indicating that the incorporation of Bi significantly improves the rate of charge transfer.

Electrocatalytic reduction of CO_2 using flow cell

After the initial tests in the H-cell, a flow cell (Fig. 3a) was used to further check eCO_2RR using Bi-ZIF-8 electrocatalysts. The gas diffusion electrode (GDE) was prepared by depositing Bi-ZIF-8 catalysts onto the gas diffusion layer (GDL). This configuration enhances the mass transport of CO_2 to the catalytic sites, overcoming the limitations associated with the H-cell (Ampelli et al. 2023). In this design, CO_2 is delivered directly to the active materials through a serpentine flow channel on the backside of the GDE. At the same time, the catholyte solution is circulated between the GDE and the membrane to optimize the overall electrochemical performance.

The flow cell tests were made at various applied potentials. Fig. 3b reports the products observed: CO, H_2, and $HCOO^-$. They were consistent with those observed in the H-cell. Additionally, trace amounts of methane were detected at −1.3 and −1.5 V vs. RHE. Notably, the flow cell achieved a higher formate yield with an FE of 80 % at a lower applied potential (compared to the H-cell) of −1.1 V vs RHE. The long-term stability of the flow cell was evaluated for 24 h, during which both the FE_{HCOO^-} and the overall stability were monitored (Fig. 3c). Moreover, the XPS was investigated after the stability as shown in Figure S4 (e and f) the Bi and Zn spectra suggesting a stable structure after the long term stability. Remarkably, the flow cell demonstrated a threefold increase in current density, reaching −150 mA cm^{-2}. The relevant increase in both the current density and FE_{HCOO^-} highlights the paramount importance of the right type of cell in studying the performances of the electrocatalysts.

The comparison of formate partial current density for both systems reveals that the H-cell achieved a maximum partial current density of −10 mA cm^{-2} at −1.2 V vs RHE. In contrast, the flow cell reached a

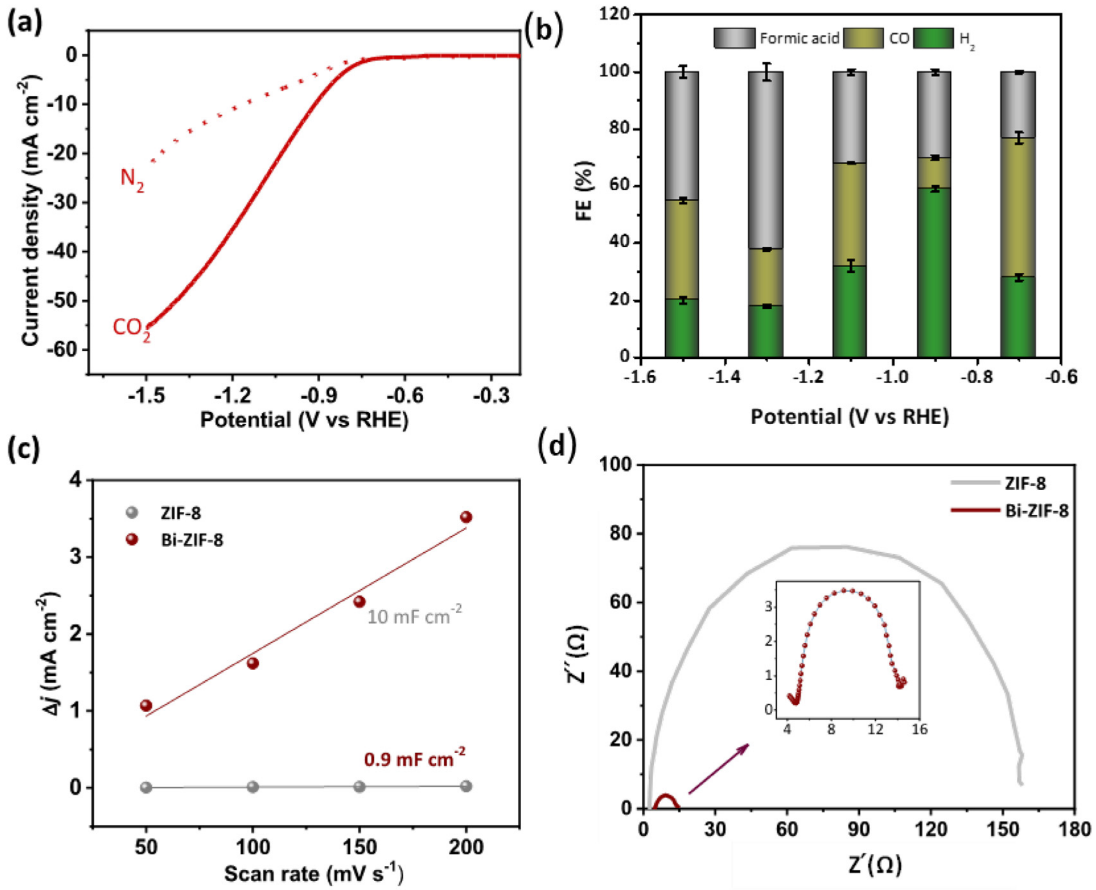

Fig. 2. (a) Linear sweep voltammetry (LSV) of Bi-ZIF-8 in 0.5 M $KHCO_3$ under N_2 and CO_2, (b) Faradic efficiency of Bi-ZIF-8 at −0.7 to −1.5 V vs RHE in 0.5 M $KHCO_3$. (c) A plot of forward peak current density vs the square root comparison of ZIF-8 and Bi-ZIF-8 with the scan rates of 50 to 200 mV/s. (d) Nyquist diagrams of ZIF-8 and Bi-ZIF-8 in 0.5 M $KHCO_3$.

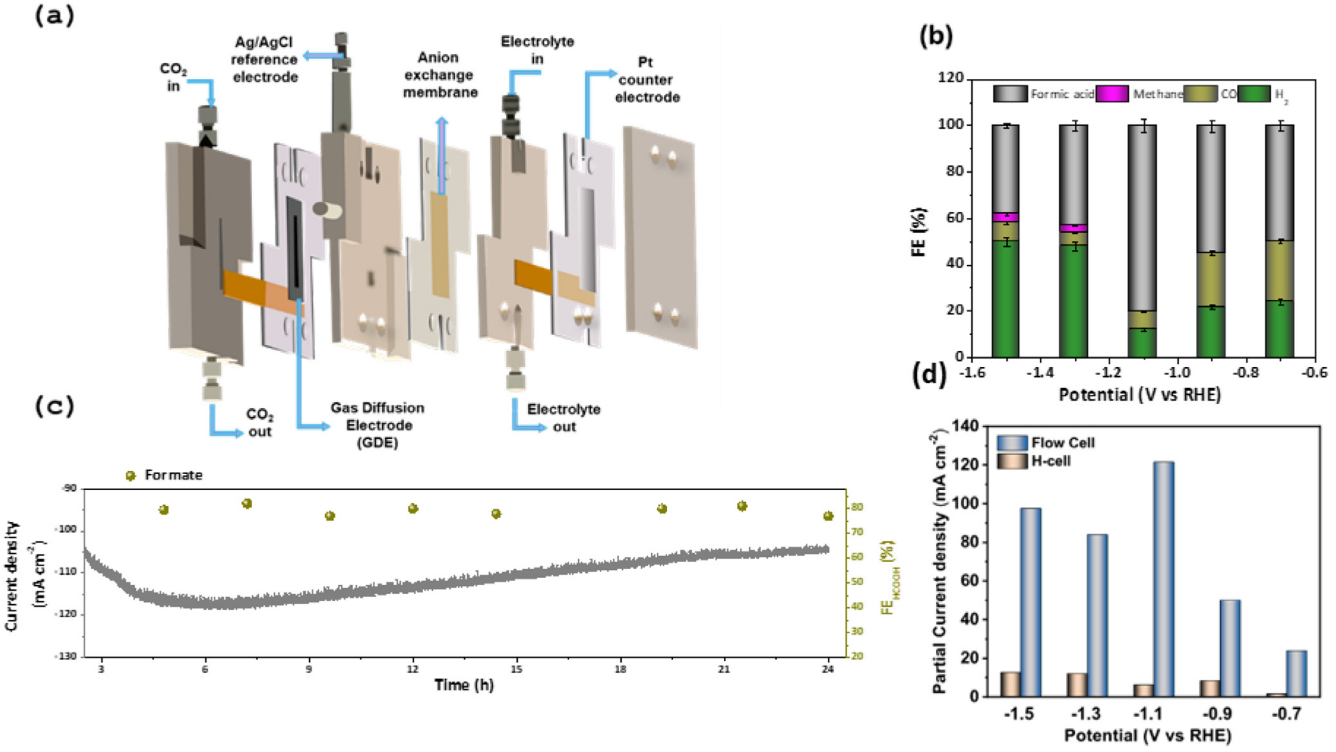

Fig. 3. (a) Schematic configuration of the flow cell. (b) Faradaic efficiency comparison of Bi-ZIF-8 at −0.7 to −1.5 V vs RHE in 1 M KOH in a flow cell. (c) Stability test of Bi-ZIF-8 using flow cell at −1.1 V vs RHE in 0.5 M $KHCO_3$. (d) Comparison of the partial current density for formate in the H-cell and flow cells.

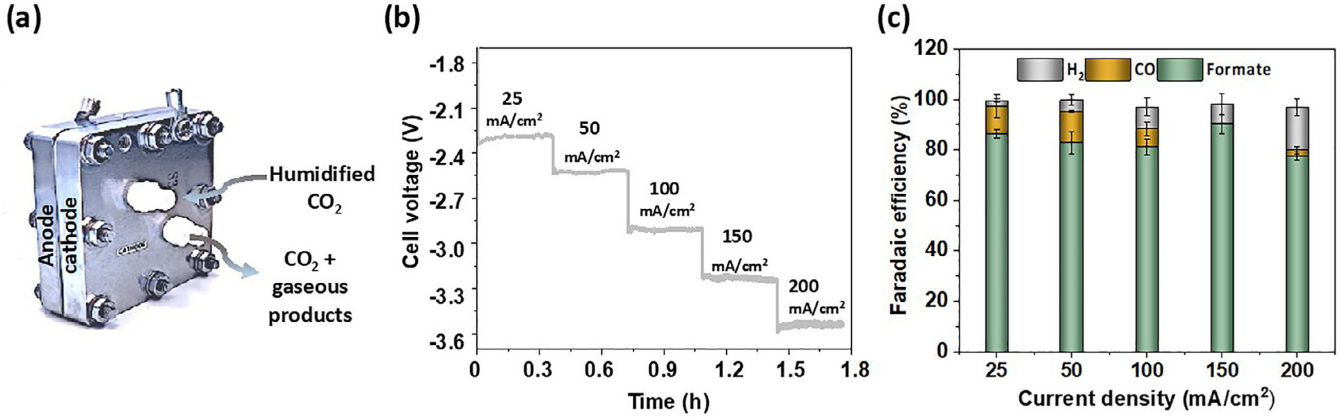

Fig. 4. (a) MEA cell for the electrochemical reduction of CO_2; (b) Stepwise plot of voltage against time at different current steps in the range of 25–200 mA cm^{-2} and (c) Faradaic efficiency of Bi-ZIF-8 using the MEA cell.

significantly higher partial current density of −120 mA cm^{-2} at −1.1 V vs RHE (Fig. 3d).

Comparing the performance of Bi-ZIF-8 in the H-cell and the flow cell, the EIS and Tafel slope shown in Figure S10a and S10b is notably lower for Bi-ZIF-8 in the flow cell. The R_{ct} value for the flow cell was 10 Ω cm^2 compared to 15 Ω cm^2 in the H-cell. Similarly, the Tafel value in the flow cell was 42 mV dec^{-1}, compared to 200 mV dec^{-1} in the H-cell. These results indicate faster kinetics for CO_2 electroreduction in the flow cell, consistently with the higher concentration of CO_2 at the surface of the electrocatalysts in the flow cell conditions. In contrast, results in the H-cell are conditioned from low CO_2 solubility in the electrolyte.

Electrocatalytic reduction of CO_2 in MEA cell

The electrocatalysts were also investigated using an MEA-type electrolyzer (Fig. 4a) to complete the comparison. Further significant differences were observed compared to H-cells and flow cells.

The MEA configuration consists of an anode chamber that contains a liquid-phase anolyte, which is positioned next to a cathode chamber that has a gas-phase intake. The moistened CO_2 is injected directly into the system as the feed, which alters the dynamics of the reaction. Stepwise constant current densities of 25 and −150 mA cm^{-2} were applied to evaluate the cell potential of Bi-ZIP-8 in the MEA cell (Fig. 4b). The cell voltage increased with the applied current density. Gas products were collected from the cathode, while liquid products were collected from the anolyte. Comparing the performance of various electrolyzers for eCO_2RR, the Bi-ZIF-8 catalyst demonstrated the highest FE_{HCOO^-} of 91 % and the highest current density of −150 mA cm^{-2} (Fig. 4c). This performance is attributed to the unique design of the MEA, which effectively enhances formate production and reduces hydrogen evolution reaction (HER) at high current densities. However, the stability of the catalyst in a zero gap MEA cell is significantly affected by the bicarbonate salt precipitation at the catalyst sites, which blocks CO_2 from reaching the catalyst sites (Endrődi et al. 2021). To further support the mechanistic understanding, we agree that comparing our findings with the literature on MEA configurations would provide valuable context (Abdinejad, Subramanian, Motlagh, Noroozifar, Duangdangchote, Neporozhnii, Ripepi, Pinto, Li and Tang 2023).

Mechanistic study

The previous results show how Bi-ZIF-8 shows excellent electrocatalytic performances (FE_{HCOO^-} > 90 % at high current density, e.g. −150 mA cm^{-2}) as well as stability. In comparison with ZIF-8, the BND considerably enhance the performance. Bi is an excellent electrocatalyst in CO_2 reduction to formate, showing high FE but typically at very low current densities of <10–20 mA cm^{-2} (Tian et al. 2021). While there is a role of the cell configuration, as commented before, the stabilization of the BND inside the ZIF-8 also plays a role in obtaining high performances, in agreement with Lamagni et al. (Lamagni et al. 2020) that claimed that nanoscale Bismuth particles stabilized by a metal-organic framework are necessary to obtain highly active and selective electrocatalysts for CO_2 reduction to formate.

To gain a better understanding of the reasons behind the high selectivity to formate, density functional theory (DFT) calculations were conducted using the Atomic Simulation Environment (ASE) (Hjorth Larsen et al. 2017). The rhombohedral structure of BND was used to construct a Bi-012 slab with lattice constants of $a = b = 4.533$ and $c = 11.797$ and three atomic layers. The details of the simulation are given in the experimental section of this paper. The optimized geometric structures of relevant adsorbates are depicted in Fig. 5a and the corresponding free energy diagrams are shown in Fig. 5b Overall, the results agree well with the literature values for the intermediate's free energies (Han et al. 2018).

As shown in Fig. 5b, the protonation of the O atom in CO_2 to form the $^*COOH$ adsorbate is significantly uphill in energy (+1.25 eV). This explains the small selectivity of BND toward CO, which is produced by the protonation of the $^*COOH$ adsorbate to produce water and CO. Similarly, the free energy of adsorption for hydrogen ($^*H$) is relatively high (+0.83 eV), which results in the suppression of hydrogen gas formation on the BND catalyst. In contrast, the protonation of the C atom in CO_2 to form the $^*HCOO$ adsorbate has a lower barrier compared with the $^*COOH$ adsorbate (1.19 eV vs 1.25 eV), which explains the higher selectivity of BND toward formic acid as compared to CO (Han et al. 2018). Upon a second proton-coupled electron transfer of the $^*HCOO$ adsorbate, the formic acid, is finally released from the catalyst surface. For more details about the free energy values of relevant adsorbates and reaction steps, refer to Tables S1-S3 in the supplementary information. These results thus evidence that the protonation of the $^*COOH$ adsorbate at O vs C atoms triggers the selectivity to CO vs formate. While the control of this path depends on the nanostructure of BND, in agreement with the great role of the nanostructure reported in the literature, it will also depend on the surface availability of protons vs chemisorbed CO_2. From here, the great role of the cell configurations. At the same time, at high current densities, e.g. the conditions for industrial applicability, the intrinsic electrocatalyst performances are overshoot by the different local environments determined by the different cell configurations. For this reason, several of the highly selective electrocatalysts at low current densities perform poorly at high current densities, and a different electrocatalyst design would be necessary to have high FE at high current densities. To further support our mechanistic analysis, the onset potential for various products was estimated using the Com-

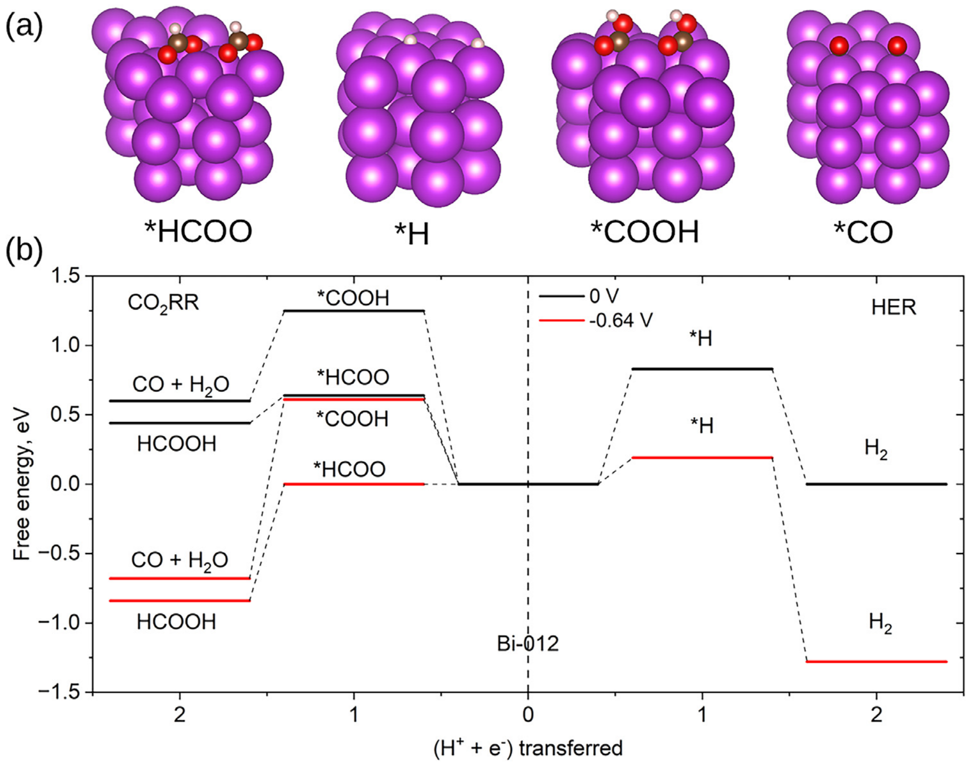

Fig. 5. DFT calculation results (a) Optimized adsorbate positions on the Bi-012 slab, (b) Free energy diagrams for H_2 evolution and CO_2 reduction to CO and HCOOH on the Bi-012 slab.

putational Hydrogen Electrode (CHE) technique and compared with the experiment findings. At higher negative potentials than −0.64 V, the free energy for * HCOO adsorbate becomes negative, making the formic acid production exergonic and thermodynamically-favored. This indeed has been observed in the experiments with significant currents starting coming only at more negative potentials than ~ −0.7 V. The other products (H_2, and CO) are endergonic at this onset potential, which explains their lower selectivity compared to HCOOH. The same trend has been observed in other studies (Han et al. 2018), showing how differences in the stability of *HCOO vs *COOH would control the selectivity toward HCOOH vs CO." Additionally, the free energy diagram has been recreated with the additional results of this analysis as shown below. The *HCOO free energy has been updated based on a more accurate calculation result. From here, the role of the ZIF-8 environment. It limits the availability of protons or assists in the protonation at C vs O atoms by hosting the BND inside the cavities. In addition, it limits their possible insitu reconstructing or sintering, allowing high stability. While further studies would be necessary to prove this indication, we believe that the present results shed new light on the factors that allow the development of high-performance CO_2 electrocatalysts compared to others reported Bi, In, and Sn-based electrocatalysts for HCOOH acid production from CO_2 as shown in Table S4.

Conclusions

Bi-ZIF-8 has been proven to be a highly effective electrocatalytic material for the CO_2 reduction to formate, particularly allowing high FE at high current density. By employing various electrochemical cells, including H-cell, flow cells, and MEA cells and conducting a systematic analysis, Bi-ZIF-8 optimized performances are of a FE of up to 91 % at −150 mA cm^{-2} using the MEA cell. This improvement is attributed to the combination of the MEA electrolyzer's design and the beneficial properties of Bi-ZIF-8 in its MOF form. While other Bi-based electrocatalysts show a high FE, it is typically at low current densities, and performances deteriorate at the high current densities requested for industrial application. Differently, the FE of Bi-ZIF-8 improves at high current densities. This difference is attributed to the role of ZIF-8, which hosts the BND inside its cavities. In this way, orienting the C vs O protonation of the $^*COOH$ adsorbate, the factor triggering selectivity. At the same time, the ZIF-8 environment protects BND from restructuring or sintering, allowing high stability.

Overall, this study highlights the potential of MOF-based electrocatalysts to advance the electrochemical conversion of CO_2 into liquid fuels, with implications for climate change mitigation and the development of sustainable energy solutions in CO_2 conversion technologies. Future research should consider further catalyst modifications, optimization of reaction parameters, and scaling up production processes to improve practical utility and economic feasibility.

Methods

Materials

Analytical grade Bismuth nitrate pentahydrate (99 %) ($Bi(NO_3)_3{\cdot}5H_2O$), zinc nitrate hexahydrate ($Zn(NO_3)_2{\cdot}6H_2O$), sodium borohydride ($NaBH_4$), and 2-methylimidazole (MeIm) were purchased from Sigma-Aldrich. All of the chemicals were analytical grade and were used without additional purification. AEM was purchased from Dioxide Materials and Membranes International, Inc. and a Nafion membrane was purchased from Fuel Cell Store.

BND-ZIF-8 synthesis

Zn $(NO_3)_2{\cdot}6H_2O$ (100 mg) was dissolved in 15 mL of deionized (DI) water. In another beaker, dissolve 70 mg of $Bi(NO_3)_3{\cdot}5H_2O$ in 15 mL DI water. In a separate beaker, 15 mL DI water was mixed with 1.94 g of 2-methylimidazole. A clear solution of $Zn(NO_3)_2{\cdot}6H_2O$ mixed with $Bi(NO_3)_3{\cdot}5H_2O$ (70 mg) solution. 2-methylimidazole was then added to the Zn and Bi solution, and the mixture was stirred for 5 min. Following that, freshly prepared 50 mg $NaBH_4$ in 2 mL DI water was quickly added to the mixture mentioned above and stirred for 5 min. Following the reaction, the products were centrifuged, washed three times with deionized water, and vacuum-dried before being used for characterization and activity analysis.

Electrode preparation

Electrode preparation for H−cell

Bi-ZIF-8 catalyst (10 mg) was distributed in a solution containing 750 µL of isopropanol, 200 µL of deionized water, and 50 µl of Nafion (5 %). The overall volume amounted to 1 mL. The solution underwent sonication for 25 min. Subsequently, a 100 µL solution was administered onto a conductive carbon paper with a 1 cm^2 surface area using the drop-casting technique. Subsequently, the sample was permitted to desiccate at ambient temperature overnight.

Electrode preparation for flow cell

The ink mentioned above for H–Cell was spray-painted on GDE (0.5 × 2 cm^2 area) using a spray gun with a constant pressure of nitrogen. The conductive surface of GDE was loaded with catalysts and dried in air, followed by vacuum drying at 50 °C.

Electrode preparation for membrane electrode assembly (MEA) cell

A mixture of the compounds (8 mg) in DMF (4 mL) with 5 wt. % Nafion was sonicated for 40 min to form a homogeneous suspension. The mixture was then stirred at room temperature overnight and drop-cast onto a gas diffusion electrode (GDE, Sigracet 38 BCE, 5 % PTFE-coated non-woven carbon paper with a microporous layer; 2.5 cm x 2.5 cm) for the MEA study.

Activity test

Activity test in H−cell

The behavior of eCO$_2$RR was initially investigated using an H-cell device (Fig. 4a) that included a silver-silver chloride (Ag/AgCl) electrode as a reference electrode. A counter electrode made of platinum mesh was used. The working electrode was affixed onto a conductive carbon paper substrate. The electrodes within the cell are linked to a Gammray 620-type potentiostat. The performance of eCO$_2$RR was evaluated using linear sweep voltammetry (LSV) techniques, which involved measuring the current densities at different applied potentials, with the current values adjusted for the electrode's geometric surface area (1 cm^2).

A suspension was made by sonicating a mixture of 5 mg of Bi-ZIF-8 catalyst in 2 mL of DMF with 2 % Nafion for 10 min to prepare the working electrode. Subsequently, 5 µL of this suspension was drop-cast onto a pre-prepared carbon paper electrode with a 1.0 cm^2 area, and allowed to dry.

Activity test in flow cell

The flow cell was employed to validate the performances under elevated current densities. The performances of eCO$_2$RR were assessed across a range of potentials (−0.7 to −1.5 V vs. RHE) during 1-hour tests. Afterwards, the liquid products were obtained from the cell and measured using ^{1}H NMR. On the other hand, the gaseous products were examined using GC-BID, namely a gas chromatograph (GC) equipped with a barrier discharge ionization detector. This detector offers a sensitivity that is two orders of magnitude greater than thermal conductivity detectors (TCD) when it comes to gas phase components.

Activity test in MEA cell

To analyze the reduced products formed in the cathodic compartment using MEA, samples from the reaction headspace were periodically collected and examined using GC. The concentrations of gaseous products (CO and H$_2$) were determined by GC, with Faradic efficiencies calculated from the average of four injections. The gaseous products from CO$_2$ electroreduction were analyzed with an InterScience PerkinElmer Clarus 680 chromatograph equipped with two TCD and a flame ionization detector (FID). For liquid products, HPLC analysis was performed using an Agilent Technologies Infinity 1260 II LC system featuring a Hi-Plex H column (at 50 °C) with a variable wavelength detector (VWD) (at 210 nm and 280 nm) and a refractive index detector (RID) at 40 °C. Proton nuclear magnetic resonance (^{1}H NMR) spectra were recorded on a Bruker 400 MHz spectrometer, and the data were analyzed using MestreNova software.

A sequence of continuous current electrolysis tests was conducted, and the gaseous substances produced by the cell were examined using an online gas chromatography system attached to the cell's outlet. The gas chromatography system was equipped with two thermal conductivity detectors and a flame ionization detector. An electrolysis process was conducted at various current densities ranging from 10 to 200 mA cm^{-2}. Each current density was maintained for 1200 s. During the reaction, aliquots were collected at 5-minute intervals, resulting in a total of four injections for each current density over 1200 s. To precisely determine the FE of products, the flow rate at the reactor output was monitored using a Bronkhorst mass flow meter.

Characterization

^{1}H and ^{13}C NMR spectra were recorded on a Bruker AM-400 spectrometer. Powdered X-ray diffraction patterns of the samples were recorded using a Rigaku MiniFlex diffractometer, which was equipped with Cu-Kα radiation. The data were acquired over the 2θ range of 5° and 30° The FT-IR spectra were obtained using a Nicolet 6700 Thermo Scientific instrument in the range of 400–4000 cm^{-1}, using KBr. The BET surface area of the MOFs was calculated by using the Micromeritics ASAP 2020 instrument. The surface morphology of these materials was discerned using a FESEM (LYRA 3 Dual Beam, Tescan), which operated at 30 kV. The surface chemical analyses were performed using an XPS equipped with an Al-Kα micro-focusing X-ray monochromator (ESCALAB 250Xi XPS Microprobe, Thermo Scientific, USA). The FESEM samples were prepared from suspension in ethanol. Potentiostat (Gammray 620, Warminster, UK) was used. Gas chromatography tests were made with Shimadzu equipment (Nexis GC-2030). Field Emission Transmission Electron Microscope was obtained from JEM-2100F, which is a multipurpose, 200 kV FE. XPS was obtained from Thermo Scientific Escalab 250Xi. The EIS was performed by varying the frequency range from 10^5 to 0.1 Hz while keeping the electrolyte and electrode conditions constant, as in the LSV experiment.

Computational study

Electronic structure calculations were performed using density functional theory (DFT) to find the lowest free energy pathways for the reduction of H_2O and CO_2 to H_2 and $CO/HCOOH$, respectively. The DFT simulations were conducted using the GPAW software, which is based on the projector augmented wave (PAW) method and the Atomic Simulation Environment (ASE). The Perdew-Burke-Ernzerhof (RBE) exchange-correlation functional, along with plane-wave pseudopotentials, were used to describe the electronic wave functions. The Bi-012 surface was modelled with lattice constants of $a = b = 4.533$ Å and $c = 11.797$ Å with three atomic layers and 10Å vacuum space. The first layer was relaxed in all directions, while the bottom two layers were fixed at the bulk equilibrium positions. The plane-wave energy cutoff was set to 500 eV with a (1,1,1) k-point sampling mesh for each lattice. The relaxation calculations were performed until the maximal force on any atom was below 0.05 $eV/$Å Multiple adsorption sites on the 012 facet, e.g. fcc and ontop binding sites, were investigated, and the lowest energy binding site was used.

Thermodynamic quantities for gas species were obtained based on the ideal gas limit by assuming that all spatial degrees of freedom are independent and separable into translational, rotational, and vibrational degrees of freedom. Vibration frequencies of adsorbates were obtained using the normal mode analysis on adsorbate atoms, assuming the harmonic approximation and considering only the vibration of adsorbate atoms. The reaction-free energies were calculated using the following relations:

$$\Delta G = \Delta H - T\Delta S \tag{1}$$

$$\Delta H = \Delta U + PV \tag{2}$$

$$\Delta U \approx \Delta E_{DFT} + \Delta E_{ZPE} + \Delta E_{Cv} + \Delta E_{solv} \tag{3}$$

where E_{DFT} is the potential energy obtained from DFT calculation, E_{ZPE} is the zero-point energy, E_{solv} is the solvation correction term.

The CHE technique was used to model the potential dependence of the free energy pathway by defining zero voltage based on the RHE. This model avoids the explicit treatment of solvated protons, and thus, a pH correction is not needed. The total chemical potential of the proton-electron pair can be expressed as a function of applied potential at all temperatures and pH values using the following relation:

$$\mu\left(H^{+}\right) + \mu(e^{-}) = \frac{1}{2}\mu\left(H_2\right) - eU \tag{4}$$

where μ is the chemical potential, e is the electron charge, and U is the applied potential. The calculation details for adsorbate-free energies can be found in Tables S1 & S2.

Declaration of competing interest

The authors declare that they have no known competing financial interests or personal relationships that could have appeared to influence the work reported in this paper.

CRediT authorship contribution statement

Muhammad Usman: Writing – original draft, Supervision, Software, Funding acquisition, Formal analysis, Data curation, Conceptualization. **Munzir H. Suliman:** Writing – review & editing, Writing – original draft, Validation, Methodology, Formal analysis, Data curation. **Maryam Abdinejad:** Writing – review & editing, Writing – original draft, Validation, Methodology, Formal analysis, Data curation. **Jesse Kok:** Writing – review & editing, Visualization, Validation, Software. **Hussain Al Naji:** Validation, Investigation, Formal analysis, Data curation. **Aasif Helal:** Writing – review & editing, Visualization, Validation, Software. **Zain H. Yamani:** Writing – review & editing, Validation, Supervision, Resources. **Gabriele Centi:** Writing – review & editing, Writing – original draft, Visualization, Validation.

Acknowledgements

The author would like to acknowledge the support provided by King Fahd University of Petroleum & Minerals (KFUPM) and the support from the Saudi Aramco Chair Professor Program at KFUPM No ORCP2390.

Supplementary materials

Supplementary material associated with this article can be found, in the online version, at doi:10.1016/j.ccst.2025.100450.

References

Abdinejad, M., Subramanian, S., Motlagh, M.K., Noroozifar, M., Duangdangchote, S., Neporozhnii, I., Ripepi, D., Pinto, D., Li, M., Tang, K., 2023. Insertion of MXene-based materials into Cu–Pd 3D aerogels for electroreduction of CO2 to formate. Adv. Energy Mater. 13 (19), 2300402.

Abdinejad, M., Subramanian, S., Motlagh, M.K., Noroozifar, M., Duangdangchote, S., Neporozhnii, I., Ripepi, D., Pinto, D., Li, M., Tang, K., Middelkoop, J., Urakawa, A., Voznyy, O., Kraatz, H.-B., Burdyny, T., 2023. Insertion of MXene-based materials into Cu–Pd 3D aerogels for electroreduction of CO2 to formate. Adv. Energy Mater. 13, 2300402.

Alenazi, M.H., Helal, A., Khan, M.Y., Khalil, A., Khan, A., Usman, M., Zahir, M.H., 2025. Covalent organic frameworks (COFs) for CO2 utilizations. Carbon Capture Sci. Technol., 100365.

Ampelli, C., Tavella, F., Giusi, D., Ronsisvalle, A.M., Perathoner, S., Centi, G., 2023. Electrode and cell design for CO2 reduction: a viewpoint. Catal. Today 421, 114217.

Askarisarvestani, G., Hoseini, S.J., Bahrami, M., Nabavizadeh, S.M., Giglio, E.De, Chen, W., 2022. Pt@ metal–organic framework (ZIF-8) thin films obtained at a liquid/liquid interface as anode electrocatalysts for methanol fuel cells: different approaches in the synthesis. Inorg. Chem. 61 (31), 12219–12236.

Bergaoui, M., Khalfaoui, M., Awadallah-F, A., Al-Muhtaseb, S., 2021. A review of the features and applications of ZIF-8 and its derivatives for separating CO2 and isomers of C3- and C4- hydrocarbons. J. Nat. Gas Sci. Eng. 96, 104289.

Boddien, A., Loges, B., Gärtner, F., Torborg, C., Fumino, K., Junge, H., Ludwig, R., Beller, M., 2010. Iron-catalyzed hydrogen production from formic acid. J. Am. Chem. Soc. 132 (26), 8924–8934.

Centi, G., Perathoner, S., 2023. The chemical engineering aspects of CO2 capture, combined with its utilisation. Curr. Opin. Chem. Eng. 39, 100879.

Chakraborty, A., Nandi, R., Kumar, D., Acharya, H., 2024. Investigation on the drug release efficacy of the Ibuprofen-loaded ZIF-8/Fe3O4 NPs nanocarrier'. ACS Omega 9 (30), 32418–32428.

Cho, J.H., Lee, C., Hong, S.H., Jang, H.Y., Back, S., Seo, M., Lee, M., Min, H.-K., Choi, Y., Jang, Y.J., Ahn, S.H., Jang, H.W., Kim, S.Y., 2023. Transition metal ion doping on ZIF-8 enhances the electrochemical CO2 reduction reaction. Adv. Mater. 35 (43), 2208224.

Costentin, C., Robert, M., Savéant, J.-M., 2013. Catalysis of the electrochemical reduction of carbon dioxide. Chem. Soc. Rev. 42 (6), 2423–2436.

Deng, P., Wang, H., Qi, R., Zhu, J., Chen, S., Yang, F., Zhou, L., Qi, K., Liu, H., Xia, B.Y., 2019. Bismuth oxides with enhanced bismuth–oxygen structure for efficient electrochemical reduction of carbon dioxide to formate. ACS Catal. 10 (1), 743–750.

Endrődi, B., Samu, A., Kecsenovity, E., Halmágyi, T., Sebők, D., Janáky, C., 2021. Operando cathode activation with alkali metal cations for high current density operation of water-fed zero-gap carbon dioxide electrolysers. Nat. Energy 6 (4), 439–448.

Fan, L., Xia, C., Zhu, P., Lu, Y., Wang, H., 2020. Electrochemical CO2 reduction to high--concentration pure formic acid solutions in an all-solid-state reactor. Nat. Commun. 11 (1), 3633.

Francke, R., Schille, B., Roemelt, M., 2018. Homogeneously catalyzed electroreduction of carbon dioxide—Methods, mechanisms, and catalysts'. Chem. Rev. 118 (9), 4631–4701.

Furukawa, H., Cordova, K.E., O'Keeffe, M., Yaghi, O.M., 2013. The chemistry and applications of metal-organic frameworks. Science 341 (6149), 1230444.

Gao, T., Wen, X., Xie, T., Han, N., Sun, K., Han, L., Wang, H., Zhang, Y., Kuang, Y., Sun, X., 2019. Morphology effects of bismuth catalysts on electroreduction of carbon dioxide into formate. Electrochim. Acta 305, 388–393.

Garba, M.D., Usman, M., Khan, S., Shehzad, F., Galadima, A., Ehsan, M.F., Ghanem, A.S., Humayun, M., 2021. CO2 towards fuels: a review of catalytic conversion of carbon dioxide to hydrocarbons. J. Environ. Chem. Eng. 9 (2), 104756.

Han, N., Wang, Y., Yang, H., Deng, J., Wu, J., Li, Yafei, Li, Yanguang, 2018. Ultrathin bismuth nanosheets from in situ topotactic transformation for selective electrocatalytic CO2 reduction to formate. Nat. Commun. 9 (1), 1320.

Hjorth Larsen, A., Jørgen Mortensen, J., Blomqvist, J., Castelli, I.E., Christensen, R., Dułak, M., Friis, J., Groves, M.N., Hammer, B., Hargus, C., Hermes, E.D., Jennings, P.C., Bjerre Jensen, P., Kermode, J., Kitchin, J.R., Leonhard Kolsbjerg, E., Kubal, J., Kaasbjerg, K., Lysgaard, S., Bergmann Maronsson, J., Maxson, T., Olsen, T., Pastewka, L., Peterson, A., Rostgaard, C., Schiøtz, J., Schütt, O., Strange, M., Thygesen, K.S., Vegge, T., Vilhelmsen, L., Walter, M., Zeng, Z., Jacobsen, K.W., 2017. The atomic simulation environment—A Python library for working with atoms. J. Phys.: Condens. Matter 29 (27), 273002.

Israr, M., Humayun, M., Suliman, M.H., Abdinejad, M., Rasheed, T., Helal, A., Khan, I., Bououdina, M., Wang, C., Usman, M., 2024. Multi-metallic electrocatalysts as emerging class of materials: opportunities and challenges in the synthesis, characterization, and applications. Catal. Rev. 1–61.

Jiang, Z., Zhang, M., Chen, X., Wang, B., Fan, W., Yang, C., Yang, Xiaoju, Zhang, Z., Yang, Xuan, Li, C., Zhou, T., 2023. A bismuth-based zeolitic organic framework with coordination-linked metal cages for efficient electrocatalytic CO2 reduction to HCOOH. Angew. Chem. Int. Ed. 62 (45), e202311223.

Lamagni, P., Miola, M., Catalano, J., Hvid, M.S., Mamakhel, M.A.H., Christensen, M., Madsen, M.R., Jeppesen, H.S., Hu, X., Daasbjerg, K., 2020. Restructuring metal–organic frameworks to nanoscale bismuth electrocatalysts for highly active and selective CO2 reduction to formate. Adv. Funct. Mater. 30 (16), 1910408.

Lee, S., Ju, H., Machunda, R., Uhm, S., Lee, J.K., Lee, H.J., Lee, J., 2015. Sustainable production of formic acid by electrolytic reduction of gaseous carbon dioxide. J. Mater. Chem. A 3 (6), 3029–3034.

Li, F., Li, Y.C., Wang, Z., Li, J., Nam, D.-H., Lum, Y., Luo, M., Wang, X., Ozden, A., Hung, S.-F., Chen, B., Wang, Yuhang, Wicks, J., Xu, Y., Li, Y., Gabardo, C.M., Dinh, C.-T., Wang, Ying, Zhuang, T.-T., Sinton, D., Sargent, E.H., 2020. Cooperative CO2-to-ethanol conversion via enriched intermediates at molecule–metal catalyst interfaces. Nat. Catal. 3 (1), 75–82.

Li, W., Yu, C., Tan, X., Ren, Y., Zhang, Y., Cui, S., Yang, Y., Qiu, J., 2024. Beyond leverage in activity and stability toward CO2 electroreduction to formate over a bismuth catalyst. ACS Catal. 14 (10), 8050–8061.

Mahbub, M.A.A., Junqueira, J.R.C., Wang, X., Zhang, J., Dieckhöfer, S., Seisel, S., Das, D., Schuhmann, W., 2024. Dynamic transformation of functionalized bismuth to catalytically active surfaces for CO2 reduction to formate at high current densities. Adv. Funct. Mater. 34 (3), 2307752.

Morales-Guio, C.G., Cave, E.R., Nitopi, S.A., Feaster, J.T., Wang, L., Kuhl, K.P., Jackson, A., Johnson, N.C., Abram, D.N., Hatsukade, T., Hahn, C., Jaramillo, T.F., 2018. Improved CO2 reduction activity towards C2+ alcohols on a tandem gold on copper electrocatalyst. Nat. Catal. 1 (10), 764–771.

Sathiyan, K., Dutta, A., Marks, V., Fleker, O., Zidki, T., Webster, R.D., Borenstein, A., 2023. Nano-encapsulation: overcoming conductivity limitations by growing MOF nanoparticles in meso-porous carbon enables high electrocatalytic performance. NPG Asia Mater. 15 (1), 18.

Schiffer, Z.J., Manthiram, K., 2017. Electrification and decarbonization of the chemical industry. Joule 1 (1), 10–14.

Shen, T., Chen, S., Zhang, C., Hu, Y., Ma, E., Yang, Y., Hu, J., Wang, D., 2022. Engineering Ir atomic configuration for switching the pathway of formic acid electrooxidation reaction. Adv. Funct. Mater. 32 (7), 2107672.

Song, Y., Yu, C., Ma, D., Liu, K., 2024. Recent progress on ZIF-8 based MOF derivatives for electrocatalysis. Coord. Chem. Rev. 499, 215492.

Suliman, M.H., Naji, H.Al, Usman, M., 2024. Zn-Cu bimetallic gas diffusion electrodes for electrochemical reduction of CO2 to ethylene. Electrochim. Acta 500, 144723.

Suliman, M.H., Usman, M., Naji, H.Al, Abdinejad, M., Ullah, N., Helal, A., Abdelnaby, M.M., Díaz-Sainz, G., Centi, G., 2025. CO2 electroreduction to C2 products on bimetallic silver copper melamine complexes. Carbon Capture Sci. Technol. 14, 100355.

Suliman, M.H., Yamani, Z.H., Usman, M., 2023. Electrochemical reduction of CO2 to C1 and C2 liquid products on copper-decorated nitrogen-doped carbon nanosheets. Nanomaterials 13 (1), 47.

Sun, D.-W., Huang, L., Pu, H., Ma, J., 2021. Introducing reticular chemistry into agrochemistry. Chem. Soc. Rev. 50 (2), 1070–1110.

Tian, Y., Li, D., Wu, J., Liu, J., Li, C., Liu, G., Chen, D., Feng, Y., 2021. Electroreduction of CO2 to formate with excellent selectivity and stability on nano-dendrite Bi film electrode. J. CO2 Util. 43, 101360.

Troyano, J., Carné-Sánchez, A., Avci, C., Imaz, I., Maspoch, D., 2019. Colloidal metal–organic framework particles: the pioneering case of ZIF-8′. Chem. Soc. Rev. 48 (23), 5534–5546.

Usman, M., Garba, M.D., Zeb, Z., Israr, M., Safia, S., Javed, F., Suliman, M.S., Alfaify, B., Sanhoob, M.A., Iqbal, N., 2023. Co2 conversion via catalytic hydrogenation to methanol, DME and syngas. In: Sustainable Utilization of Carbon Dioxide: From Waste to Product. Springer, pp. 37–59.

Usman, M., Suliman, M.H., 2023. Silver-doped zeolitic imidazolate framework (Ag@ ZIF-8): an efficient electrocatalyst for CO2 conversion to Syngas. Catalysts 13 (5), 867.

Usman, M., Suliman, M.H., Salihu, I.M., Ullah, N., Abdelnaby, M.M., Abdelsamie, M., 2025. Cadmium Functionalized Zeolitic Imidazolate framework (Cd-ZIF-8) electrocatalysts for efficient CO2 conversion to Syngas. ACS Omega.

Wang, X., Wang, Z., García de Arquer, F.P., Dinh, C.-T., Ozden, A., Li, Y.C., Nam, D.-H., Li, J., Liu, Y.-S., Wicks, J., Chen, Z., Chi, M., Chen, B., Wang, Y., Tam, J., Howe, J.Y., Proppe, A., Todorović, P., Li, F., Zhuang, T.-T., Gabardo, C.M., Kirmani, A.R., McCallum, C., Hung, S.-F., Lum, Y., Luo, M., Min, Y., Xu, A., O'Brien, C.P., Stephen, B., Sun, B., Ip, A.H., Richter, L.J., Kelley, S.O., Sinton, D., Sargent, E.H., 2020. Efficient electrically powered CO2-to-ethanol via suppression of deoxygenation. Nat. Energy 5 (6), 478–486.

Wu, Y., Jiang, Z., Lu, X., Liang, Y., Wang, H., 2019. Domino electroreduction of CO2 to methanol on a molecular catalyst. Nature 575 (7784), 639–642.

Xu, Y., Zhang, M., Tian, T., Shang, Y., Meng, Z., Jiang, J., Zhai, J., Wang, Y., 2015. Mimicking how plants control CO2 influx: CO2 activation of ion current rectification in nanochannels. NPG Asia Mater. 7 (9) e215.

Yaghi, O.M., Kalmutzki, M.J., Diercks, C.S., 2019. Introduction to Reticular chemistry: Metal-Organic Frameworks and Covalent Organic Frameworks. John Wiley & Sons.

Yang, S., Jiang, M., Zhang, W., Hu, Y., Liang, J., Wang, Y., Tie, Z., Jin, Z., 2023. In situ structure refactoring of bismuth nanoflowers for highly selective electrochemical reduction of CO2 to formate. Adv. Funct. Mater. 33 (37), 2301984.

Yao, D., Tang, C., Vasileff, A., Zhi, X., Jiao, Y., Qiao, S., 2021. The controllable reconstruction of Bi-MOFs for electrochemical CO2 reduction through electrolyte and potential mediation. Angew. Chem. 133 (33), 18326–18332.

Zhao, J., Yang, Q., Shi, R., Waterhouse, G.I.N., Zhang, X., Wu, L.-Z., Tung, C.-H., Zhang, T., 2020. FeO–CeO2 nanocomposites: an efficient and highly selective catalyst system for photothermal CO2 reduction to CO. NPG Asia Mater. 12 (1), 5.

Zulkifli, Z.I., Lim, K.L., Teh, L.P., 2022. Metal-organic frameworks (MOFs) and their applications in CO2 adsorption and conversion. ChemistrySelect 7 (22), e202200572.